

Partial melting of the Indarch (EH4) meteorite: A textural, chemical, and phase relations view of melting and melt migration

TIMOTHY J. MCCOY^{1*}, TAMARA L. DICKINSON² AND GARY E. LOFGREN³

¹Department of Mineral Sciences, National Museum of Natural History, Smithsonian Institution, Washington, D.C. 20560-0119, USA

²Physics Department, Catholic University of America, Washington, D.C. 20064, USA

³Code SN2, NASA/Johnson Space Center, Houston, Texas 77058, USA

*Correspondence author's e-mail address: mccoym.tim@nmnh.si.edu

(Received 1998 August 13; accepted in revised form 1999 May 28)

Abstract—To test whether aubrites can be formed by melting of enstatite chondrites and to understand igneous processes at very low O fugacities, we have conducted partial melting experiments on the Indarch (EH4) chondrite at 1000–1500 °C. Silicate melting begins at 1000 °C, and Indarch is completely melted by 1500 °C. The metal–sulfide component melts completely at 1000 °C. Substantial melt migration occurs at 1300–1400 °C, and metal migrates out of the silicate charge at 1450 °C and ~50% silicate partial melting. As a group, our experiments contain three immiscible metallic melts (Si-, P-, and C-rich), two immiscible sulfide melts (Fe- and FeMgMnCa-rich), and silicate melt. Our partial melting experiments on the Indarch (EH4) enstatite chondrite suggest that igneous processes at low fO_2 exhibit several unique features. The complete melting of sulfides at 1000 °C suggests that aubritic sulfides are not relics. Aubritic oldhamite may have crystallized from Ca and S complexed in the silicate melt. Significant metal–sulfide melt migration might occur at relatively low degrees of silicate partial melting. Substantial elemental exchange occurred between different melts (e.g., S between sulfide and silicate, Si between silicate and metal), a feature not observed during experiments at higher fO_2 . This exchange may help explain the formation of aubrites from known enstatite chondrites.

INTRODUCTION

Enstatite meteorites represent an ideal opportunity to investigate the range of igneous processes acting on a common precursor throughout the history of the solar system. This group, which is linked by a common O-isotopic signature (Clayton *et al.*, 1984) includes chondrites (EL, EH); impact-melt rocks, breccias, and clasts from the EL and EH chondrite parent bodies; achondrites (aubrites); stony-iron meteorites; and iron meteorites. Enstatite meteorites are highly reduced, containing virtually FeO-free silicates. In addition, normally lithophile elements behave as chalcophile and siderophile elements, producing a variety of sulfide phases (e.g., oldhamite-CaS, ningerite-MgS, daubreelite-FeCr₂S₄), and Si-bearing metal.

Although a tentative link exists between enstatite chondrites and aubrites, there are important differences in the chemistry and mineralogy of these groups that lead to a number of unanswered questions. These include: (a) Can aubrites form from known enstatite chondrites? A number of important differences exist between aubrites and known enstatite chondrites, including the presence in aubrites of abundant forsterite (Waters and Prinz, 1979), inverted pigeonite (Taylor *et al.*, 1988), and Ti-rich troilite (Brett and Keil, 1986). It is difficult to explain the presence of these phases in aubrites by melting of enstatite chondrites using known phase relationships (Taylor *et al.*, 1988). (b) What happened to the basaltic partial melts? Abundant basaltic partial melts should be generated during melting of enstatite chondrites, but basaltic clasts are remarkably scarce within aubrites. Experimental studies can help to define the expected compositions of these partial melts. (c) Is aubritic oldhamite a nebular relic or a product of igneous crystallization? Oldhamite, which is the major rare-earth-element (REE) carrier in enstatite meteorites, has an extraordinarily high melting temperature as a pure substance (~2525 °C). Aubritic oldhamites have a diverse range of REE patterns in aubrites, some of which are similar to those in unequilibrated enstatite chondrites (Floss and

Crozaz, 1993; Crozaz and Lundberg, 1995). This has led to the suggestion that some aubritic oldhamite is a nebular relic that survived igneous processing. However, textural evidence (Wheelock *et al.*, 1994) and REE patterns in some aubritic oldhamite favor an igneous origin (Floss and Crozaz, 1993). To date, the melting behavior of oldhamite in a complex, multiphase system such as an enstatite chondrite has not been established.

In addition to their unique chemical features, these meteorites also exhibit unusual textural features. With the exception of Shallowater, aubrites are breccias composed of igneous clasts, with the vast majority of the clasts composed of nearly-pure enstatite up to 10 cm in length (Lonsdale, 1947). Adjacent enstatites often exhibit ragged intergrowths suggestive of cocrystallization (Taylor *et al.*, 1993). In addition, many aubrites are depleted in plagioclase, metal, and troilite (Watters and Prinz, 1979). The metal that is present sometimes occurs as large, spherical nodules, suggestive of formation as an immiscible melt (Casanova *et al.*, 1993). Finally, aubrites often contain exsolution phases, such as daubreelite in troilite, and perryite and schreibersite in metal. Taken together, these features suggest that aubrites experienced a relatively prolonged thermal history with high degrees of partial melting, melt migration, crystallization, and slow cooling.

Despite extensive petrologic studies of aubrites, few experimental studies on the melting of enstatite chondrites have been conducted. This is due in large part to the difficulty of reproducing these highly reducing conditions. Preliminary studies have been reported by Dickinson and Lofgren (1992), Fogel *et al.* (1996), McCoy *et al.* (1997), Dickinson *et al.* (1998), and McCoy *et al.* (1998). We report here the results of partial melting experiments on the Indarch (EH4) enstatite chondrite conducted at temperatures covering the entire range of partial melting (1000–1500 °C). We examine the chemical, textural, and phase relationships of these experiments with applications to the genesis of aubritic meteorites.

EXPERIMENTAL TECHNIQUES

Several grams of interior, unweathered material were obtained from the 27 kg Indarch meteorite (Me 1404, Field Museum of Natural History, Chicago), coarsely ground, and stored in a vacuum oven at 110 °C. Indarch is intrinsically reduced, and this reduced state was maintained during the experiments using graphite crucibles and solid metal buffers. Aliquots of ~160 mg of powdered Indarch were placed in graphite crucibles (99+% pure on metals basis). The solid metal buffers (Cr powder or V chips) were placed in an Al₂O₃ crucible. The Cr metal maintained the intrinsically low O fugacities at temperatures ≥1200 °C. However, at lower temperatures, the Cr metal became highly chalcophile and, thus, the charges contained no sulfides. At 1000–1100 °C, a V-metal buffer maintained the low O fugacity but was too reducing at higher temperatures. Both crucibles were sealed in an evacuated silica tube. Thus, the sample should stay at the Cr–Cr₂O₃ or V–V₂O₃ buffer depending on the buffer utilized, which closely duplicates the intrinsic O fugacity of enstatite chondrites. A schematic representation of the experimental setup is shown in Fig. 1.

Experiments were run in gas-mixing furnaces with CO–CO₂ gas maintained near the iron–wüstite buffer to increase the stability of the silica tubes. Experimental run times ranged from 4–24 h at 1000–1500 °C and were selected to provide balance between establishing chemical equilibrium and minimizing volatile loss, particularly of S. Temperatures were measured using type B thermocouples (Pt₉₄Rh₆–Pt₇₀Rh₃₀) calibrated against the melting point of Au and are accurate to ±5 °C. Preliminary experiments (McCoy *et al.*, 1997) suggested that longer run times (*e.g.*, 120 h) produced unacceptably high volatile loss. Samples were quenched using compressed air and cooled to below the solidus in about one minute.

After the experiments, each buffer contained both the metal and metal–oxide phase as determined by optical microscopy and energy dispersive analyses on the scanning electron microscope, indicating Indarch's low intrinsic O fugacity was maintained. Moderate Si concentrations in the metal and low FeO concentrations in the silicate minerals and glass also suggest that reducing conditions were maintained. In addition to the metal and metal–oxide, several buffers contain S- and Al-rich phases, undoubtedly owing to reaction with volatilized S from the charge and Al₂O₃ from the crucible, respectively. To avoid hydration and loss of CaS, all samples were cut and polished using oil and stored in dessicators. Definitive identification of phases, and analyses of their compositions, was confirmed using a JEOL JXA 8900R electron microprobe.

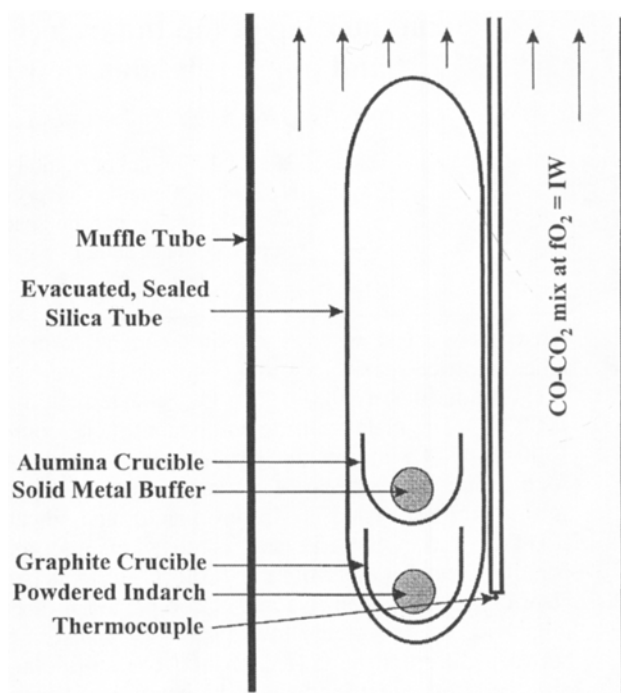


FIG. 1. Schematic of the experimental setup used in our experiments.

Microprobe analyses used a 15 keV accelerating potential and 20 nA beam current. A fully focused beam was used for metal and sulfides. Glass analyses used a rastered beam with spot sizes of 1–10 μm. A small spot size was necessary in the low-temperature runs owing to the small size of the glass pockets. Standards used for metal were Fe–Si alloy (Si), Fe–Ni alloy (Ni), pure Fe and Co, schreibersite (P), and troilite (S); for sulfides were troilite (Fe,S), Kakanui Hornblende (Mg,Ca), ilmenite (Ti), pure Mn and Cr; and for silicates were Kakanui Hornblende (Al,Fe,Mg,Ca,Na,K,Ti), bytownite (Si), manganite (Mn), apatite (P), chromite (Cr), and scapolite (S). Carbon was analyzed using samples of graphite, an Fe standard, and the Indarch samples all C coated at the same time. After standardization on graphite, the pure Fe standard was analyzed for C to assess the contribution of C from the carbon coat. This quantity (~3.9 wt%) was subtracted from each individual analyses of Indarch metal. Although uncertainties in this type of analyses are large, some Indarch metal was enriched in C by more than 3 wt% relative to the Fe standard. Relative homogeneity of phases within individual charges suggests that chemical equilibrium was approached.

TABLE 1. Experimental run conditions and summary of phases present in experimental charges.

| Run No. | T (°C) | t (h) | B | Fe Ni Si-rich metal | P-rich metal | C-bearing metal | Fe-rich sulfide | Fe Mn Mg Ca-rich sulfide* | Fe | En | Fe Cr Ca-rich En | Plag | Melt | SiO ₂ |
|---------|--------|-------|----|---------------------|--------------|-----------------|-----------------|---------------------------|----|----|------------------|------|------|------------------|
| 284 | 1500 | 4 | Cr | x | r | — | — | — | — | — | — | — | x | — |
| 285 | 1450 | 16 | Cr | x | r | — | — | — | x | x | — | — | x | — |
| 262 | 1425 | 20 | Cr | x | — | x | x | x | x | x | — | — | x | — |
| 269 | 1400 | 24 | Cr | x | — | x | x | x | x | x | — | — | x | — |
| 278 | 1300 | 24 | Cr | x | r | x | x | x | — | x | — | — | x | m |
| 261 | 1200 | 24 | Cr | x | r | x | x | x | — | x | m | — | x | m |
| 291 | 1100 | 24 | V | x | — | — | x | x | r | x | m | m | x | r |
| 286 | 1000 | 24 | V | x | — | — | x | x | — | x | m | m | — | r |
| Indarch | — | — | — | o | o | — | o | o | — | o | o | o | — | o |

* Proportions of cations vary. See text for discussion. B = solid metal buffer.

Abundance of phases: x = abundant (>5 vol%), m = minor (1–5 vol%), r = rare (<1 vol%), o = occurs in Indarch.

Experimental run conditions are shown in Table 1, along with the phases present in each charge. Modal analyses of 400–650 points per charge were conducted using a Nikon microscope in reflected and transmitted light and employing a Hennig ocular.

RESULTS

Indarch consists of enstatite, plagioclase, free SiO_2 , FeO-bearing pyroxene, Fe,Ni metal, troilite, schreibersite, niningerite, oldhamite, daubreelite, and graphite (Keil, 1968; this work) (Table 1). Detailed textural descriptions of our melting experiments are given in the appendix and chemical compositions of the metal, sulfide, and silicate melts in Tables 3–5.

Textural Changes During Melting

With increasing temperature, we observe decreasing porosity in the experimental charges and increasing degrees of silicate partial melting (Fig. 2a–d, Table 2). We did not observe metal, sulfide, or

silicate melts permeating into or reacting with the graphite crucible at any temperature. At 1400 °C, silicate partial melting has reached ~20%, and the charge is ellipsoidal with no appreciable void space (Fig. 2c). At 1100–1425 °C, silicate partial melt occurs interstitially to mafic silicates throughout the volume of the charge (Fig. 3). Even with increasing degrees of partial melting, we do not observe substantial silicate melt migration within the charges (*e.g.*, to the edge or concentrating in millimeter-sized, crystal-free areas). At 1425 °C, forsterite occurs preferentially at the rim of the charge, which possibly suggests some movement of melt to the surface. With increasing temperature, we also observe an apparent coarsening of the residual enstatite grains. This is particularly true at 1425 °C, where residual enstatite seems considerably larger (a few hundred microns; Fig. 4a) than at lower temperatures, probably as the result of crystallization of enstatite from the partial melt as the system attempts to reach equilibrium. At 1450 °C, the charge contains 1 or 2 enstatite and 2–4 barred olivine crystals, each of which approaches

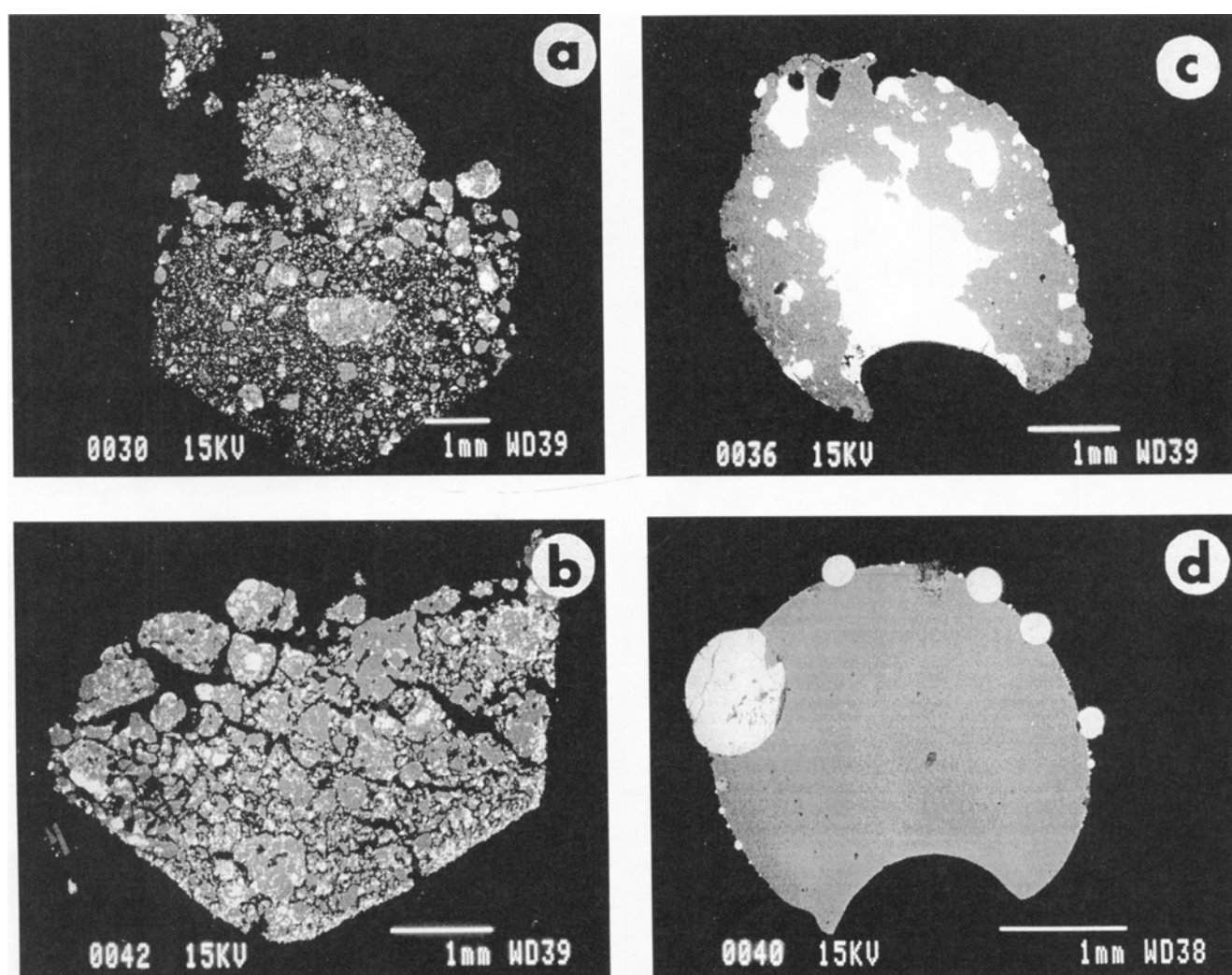


FIG. 2. Large-scale textures of Indarch partial melting experiments shown in backscattered electron images. (a) The 1000 °C charge exhibits no silicate partial melting and ~50% void space. The abundant void space is a result of grinding and preparing the powder and is not intrinsic to Indarch. Fine-grained metallic, iron-sulfide and mixed sulfide melts occur as distinct particles. (b) At 1200 °C, silicate partial melting and sintering has produced a coherent charge. (c) At 1400 °C, ~20% partial melting produces a spherical charge with no void space. Millimeter-sized metal-sulfide particles occur throughout the charge, typically with cores of metal and rims of sulfides. (d) Complete silicate partial melting has occurred at 1500 °C. Sulfide is nearly absent, having dissolved into the silicate melt, and metal has migrated to the edge of the charge, forming metallic spheres on the edge of the silicate sphere. The large indentation in the silicate sphere was left when a large metal sphere separated from the charge.

TABLE 2. Modal analyses of Indarch partial melting experiments.

| Run No. | T (°C) | t (h) | Voids (vol%) | Silicate partial melting (vol%) | Metallic melt (wt%) | Sulfide melt (wt%) |
|---------|--------|-------|--------------|---------------------------------|---------------------|--------------------|
| 284 | 1500 | 4 | 0 | 100 | 38 | trace |
| 285 | 1450 | 16 | 0 | 46 | 45 | 0 |
| 262 | 1425 | 20 | 0 | 29 | 33 | 6 |
| 269 | 1400 | 24 | 0 | 20 | 21 | 10 |
| 278 | 1300 | 24 | 25 | 19 | 26 | 15 |
| 261 | 1200 | 24 | 36 | 9 | 23 | 13 |
| 291 | 1100 | 24 | 53 | 7 | 31 | 10 |
| 286 | 1000 | 24 | 52 | 0 | 27 | 19 |

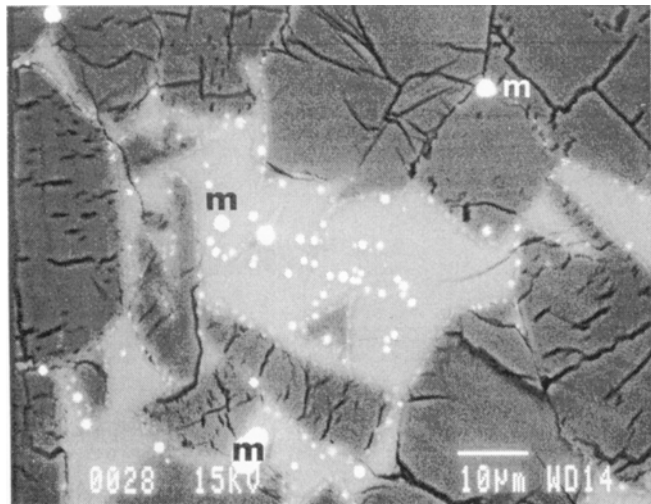


FIG. 3. At 1425 °C, small (1–2 μm) Ca-rich sulfides occur in the silicate melt, often lining large enstatite crystals. A few larger metal grains (m) are also present. These Ca-rich sulfides appear to have crystallized from the silicate melt, supporting the idea of Fogel *et al.* (1996) that aubritic oldhamite may have crystallized from the silicate melt.

1 mm in maximum dimension (Fig. 4b). By 1500 °C, the charge is completely melted and crystallized into numerous pyroxene spherulites (Figs. 2d and 4c).

At 1000 °C, the three nonsilicate melt components (FeNiSi metallic, Fe-sulfide, and Fe,Ca,Mg,Cr,Mn-sulfide) occur as distinct, highly irregular grains of a few tens of microns in size distributed throughout the volume of the charge (Fig. 2a). The boundary between the two sulfide melts is sometimes concave, typical of immiscible melts. From 1100–1400 °C, the number of nonsilicate melt components increases, and their intergrowths become more complex, although these changes occur gradually with increasing temperature. It should be noted that some of the textural complexity almost certainly results from cooling of these charges. At 1200–1425 °C, the metal is a two-phase intergrowth of FeNiSi and C-bearing metal, with the latter forming a network into which islands of the former are embedded. The P-rich metal is observed as a rare phase at temperatures ranging from 1200–1500 °C. At 1300–1425 °C, the iron-sulfide melt sometimes contains stringers of metallic melt and skeletal and cruciform Fe,Mg,Mn,Ca,Cr-rich sulfide (Fig. 5). Up to 1300 °C, metal and sulfide particles remain quite small (typically <100 μm) and are uniformly distributed throughout the charge. Between 1300 and 1400 °C, we see a sudden and dramatic change in the distribution of metal. Metallic and sulfide melts at 1400 °C and above occur as large (0.5–3 mm) compound particles distributed throughout the volume of the charge (Fig. 2c). Segregation of metal into large

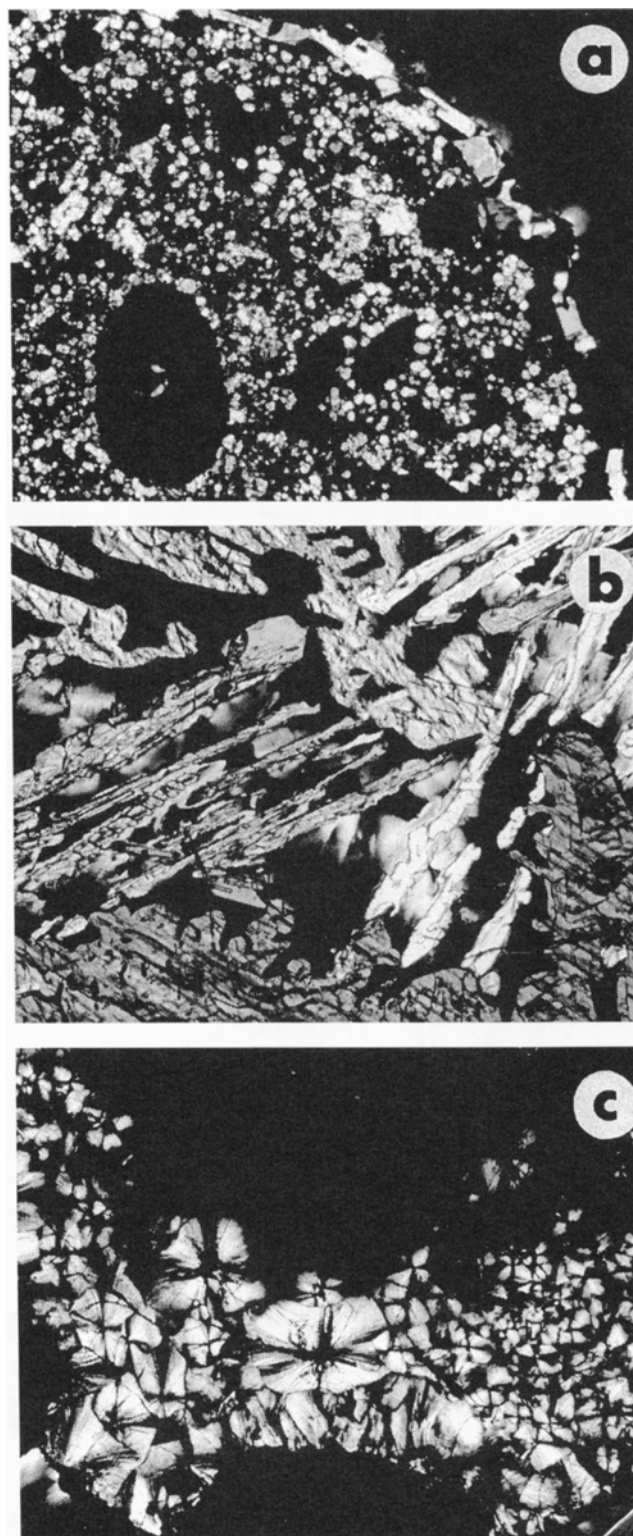


FIG. 4. The effects of crystallization on the silicate textures of the charges. All are photomicrographs in transmitted, cross-polarized light. Field of view of each is 2.6 mm. (a) At 1425 °C, the charge contains abundant striated enstatites of a few hundred microns in size, reflecting the abundance of nuclei during crystallization. (b) At 1450 °C, the charge contains 1 or 2 enstatite grains and 2–4 barred olivines, each of which approaches 1 mm in maximum dimension. This texture reflects the low nuclei density of the charge. (c) By 1500 °C, all preexisting nuclei have been destroyed during complete melting and the charge crystallized into numerous spherulites.

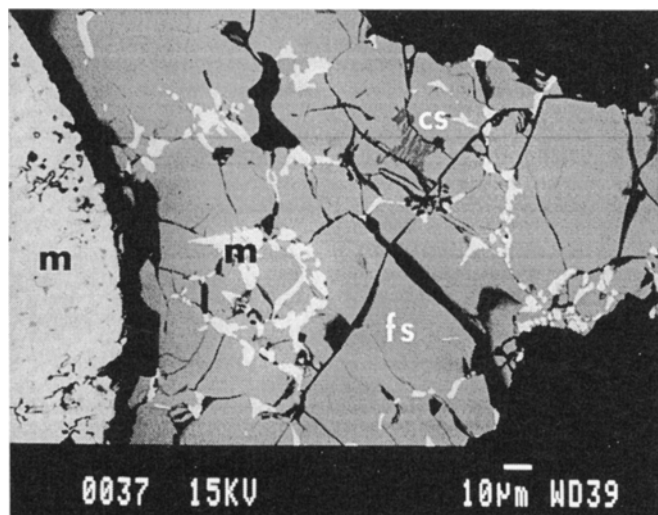


FIG. 5. Backscattered electron image of the complex metal-sulfide assemblage present at 1400 °C. The large central metal particle (m) is composed of islands of FeNiSi metallic melt in a C-bearing metallic melt. The rimming Fe-rich sulfide (fs) contains stringers of metal (m) and skeletal to cruciform complex FeMgMnCaCr-rich sulfides (cs). These textures may have partially formed upon cooling of the experimental charge.

particles occurs at ~25 vol% silicate partial melting. Above 1400 °C, near the edge of the charge, sulfides are rare and the C-bearing metal is often absent. In the center of the charge, metallic spheres often have mantles of sulfide melts. In the 1400–1500 °C charges, small (1–2 µm) gray sulfides (Fig. 3) are associated with the silicate melt and occur at the edges of silicate crystals. Although these sulfides were too small for reliable quantitative analyses, qualitative analyses suggest they are enriched in Ca and S. At 1450 and 1500 °C, sulfide is virtually absent in these charges, and spheres of metallic melt occur on the surface of the silicate sphere (Fig. 2d). This migration of the metallic melt to the edges of the charge occurs at ~50% silicate partial melting (Table 2). The decrease in modal sulfide abundance (Table 2) from 1400–1500 °C is consistent with the increase in S abundance in the silicate melt, as discussed below.

Chemical Changes During Melting

All charges contain Fe,Ni,Si-rich metal with Si ranging between 1.5 and 15.1 wt%, confirming the reduced nature of the charges.

Metal in Indarch contains 3.5 wt% Si (Keil, 1968). The composition of the Fe,Ni,Si-rich metal remains relatively constant to 1425 °C; and then Fe decreases significantly, Ni decreases, and Si increases with increasing temperature (Table 3, Fig. 6). This may represent the reduction of SiO₂ in the silicate melt to Si in the Fe,Ni,Si-rich metallic liquid. The buffer is instrumental in forcing a low O fugacity and, thereby, causing the reduction of SiO₂ in the silicate melt. Oxidation of graphite, either indigenous to Indarch or more likely from the crucible, may also have contributed to this reduction. Because Indarch contains only 0.04 wt% graphite (Keil, 1968), this process could occur in nature on a much smaller scale. At all temperatures, the Si-rich metallic melt is low in Cr, Co, P, and S. The P-rich metal (up to 13.0 wt% P) is rare and probably represents the melting of schreibersite (Keil, 1968) that was present in Indarch (Tables 1 and 3). The C-bearing metal contains up to 3.3 wt% C and occurs in the intermediate temperature runs (1200–1425 °C) as an intimate intergrowth with FeNiSi metallic melt (Table 3).

All charges from 1000–1425 °C contain quenched Fe-rich sulfide liquid with minor amounts (wt% levels) of Cr, Mn, and Ni (Table 4). No sulfides were observed in any of the sections of the 1450 °C charge. The absence of sulfides in this charge, combined with the low abundance of S in the silicate melt (Table 5), suggests excess volatilization in this charge. It is unclear what caused the excess volatilization, which occurred even though the silica tube did not appear to fail. Examination of the silica tubes in the scanning electron microscope suggests condensation of volatile-rich (e.g., Na,S) phases in the cooler, upper end of the silica tube. The use of shorter tubes was not possible, owing to the risk of substantial heating of the charge during sealing of the tube. In most cases, a constant S vapor pressure appears to have been established, preventing evaporation of all S from the charge. The 1000–1425 and 1500 °C charges contain a quenched Fe,Mn,Mg,Ca,Cr-rich sulfide liquid; and at 1200 °C, two mixed sulfide melts of slightly different composition were observed (Table 4). The Ca and Mg concentrations in the mixed sulfide melt increase from 1000–1200 °C and then decrease at higher temperature (Fig. 7). Iron, Mn, and Cr exhibit the opposite trend. The cause of the complementary variations of Fe, Mn, and Cr with Mg and Ca in the sulfide melt is unclear but may reflect exchange of Ca and Mg between sulfide and silicate melts (as discussed later) or the change in the buffer (V vs. Cr).

TABLE 3. Quenched liquid metal compositions reported in elemental weight percent.

| T | N | Fe | Ni | Si | P | C | S | Co | Cr | Total |
|------|----|------------|-------------|-------------|-------------|-----------|-------------|-------------|-------------|--------|
| 1500 | 18 | 78.9 (0.8) | 4.03 (0.19) | 15.1 (0.29) | 0.14 (0.02) | ND | BD | 0.23 (0.03) | 0.78 (0.04) | 99.21 |
| | 4 | 71.2 (0.9) | 3.95 (0.27) | 8.67 (0.70) | 11.5 (1.2) | ND | 0.06 (0.03) | 0.21 (0.01) | 3.16 (0.23) | 98.75 |
| 1450 | 20 | 85.0 (0.7) | 4.86 (0.19) | 7.65 (0.51) | 0.20 (0.15) | ND | BD | 0.23 (0.04) | 0.92 (0.16) | 98.84 |
| | 4 | 70.9 (1.5) | 4.79 (0.10) | 3.01 (0.58) | 13.0 (1.1) | ND | BD | 0.26 (0.02) | 5.42 (0.50) | 97.42 |
| 1425 | 8 | 86.3 (1.0) | 6.04 (0.70) | 5.11 (0.22) | 0.13 (0.27) | ND | 0.05 (0.13) | 0.29 (0.06) | 0.34 (0.13) | 98.30 |
| | 12 | 92.7 (1.3) | 2.07 (1.72) | 0.82 (1.74) | BD | 3.3 (1.2) | BD | BD | ND | 98.97 |
| 1400 | 13 | 87.2 (1.3) | 6.90 (0.73) | 5.41 (0.75) | 0.14 (0.06) | ND | BD | 0.31 (0.04) | 0.16 (0.02) | 100.16 |
| | 20 | 89.6 (3.0) | 4.58 (2.54) | 2.12 (1.64) | 0.92 (1.18) | 1.8 (1.4) | 0.36 (0.83) | BD | ND | 99.42 |
| 1300 | 9 | 87.0 (0.7) | 6.51 (0.54) | 4.69 (0.43) | 0.12 (0.06) | ND | BD | 0.37 (0.04) | 0.19 (0.08) | 98.87 |
| | 10 | 86.6 (3.7) | 4.46 (1.71) | 1.27 (0.81) | 4.51 (3.27) | 2.2 (1.5) | 0.15 (0.10) | BD | ND | 99.26 |
| | 5 | 82.8 (1.3) | 5.51 (0.38) | 2.23 (0.70) | 7.60 (1.82) | ND | 0.14 (0.38) | 0.28 (0.04) | 0.26 (0.12) | 98.80 |
| 1200 | 16 | 87.6 (1.4) | 6.65 (0.75) | 5.16 (0.49) | 0.19 (0.22) | ND | BD | 0.35 (0.04) | 0.07 (0.04) | 99.99 |
| | 13 | 85.6 (3.6) | 5.66 (1.39) | 2.76 (1.49) | 4.9 (3.66) | 1.3 (1.4) | 0.18 (0.11) | BD | ND | 100.48 |
| | 2 | 83.9 (0.3) | 5.50 (0.04) | 1.84 (0.01) | 8.51 (0.94) | ND | 0.27 (0.01) | 0.29 (0.01) | 0.06 (0.01) | 100.37 |
| 1100 | 10 | 89.0 (0.7) | 5.96 (0.35) | 3.04 (0.06) | 0.31 (0.03) | ND | BD | 0.32 (0.02) | ND | 98.65 |
| 1000 | 10 | 90.6 (0.8) | 6.26 (0.45) | 1.48 (0.02) | 0.63 (0.04) | ND | BD | 0.31 (0.04) | ND | 99.33 |

Average ($\pm 1\sigma$). T = temperature in °C. N = number of analyses. ND = not determined. BD = below detection limit (typically 0.03 wt%).

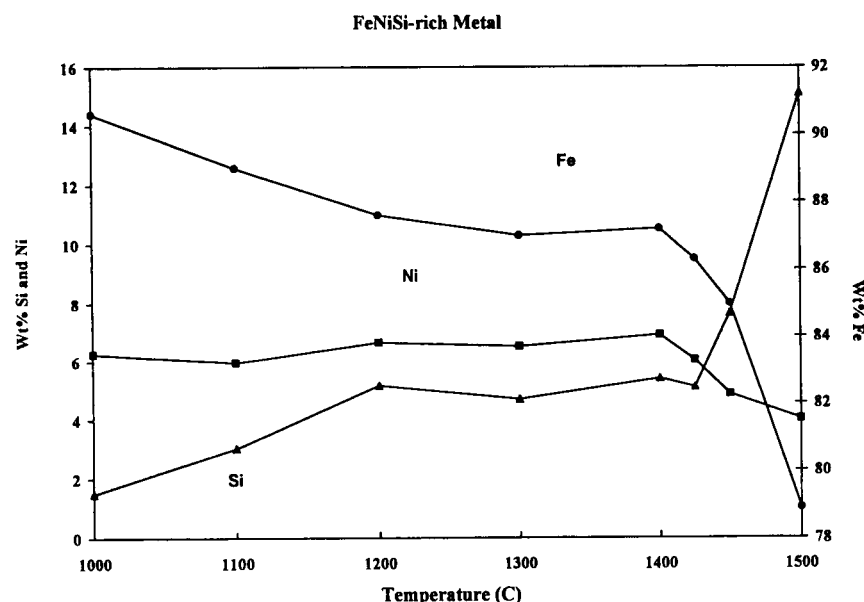


FIG. 6. Temperature vs. average elemental abundance for the FeNiSi-rich metal. Fe is plotted on the right axis and Si and Ni on the left axis. Iron decreases and Si increases with increasing temperature above 1425 °C representing the reduction of SiO_2 in the silicate melt to Si in the FeNiSi-rich metallic liquid, perhaps accompanied by the oxidation of graphite, either from the crucible or indigenous to Indarch.

No relic sulfides from the starting composition (oldhamite, niningerite, and troilite) were observed in the charges at any temperature.

The 1000 °C charge exhibits no indications of silicate partial melting. This assemblage contains enstatite (0.8 ± 0.4 wt% FeO), plagioclase of two compositions (Ab_{93} and Ab_{51}), Fe,Cr,Ca-rich pyroxene (6.4 wt% FeO, 1.2 wt% CaO, 1.4 wt% Cr_2O_3), and SiO_2 . Similar compositions for enstatite (0.84 wt% FeO) and plagioclase ($\text{Ab}_{97.6}$) were reported by Keil (1968). At 1100 °C, albitic plagioclase is absent, and a very small quantity of silicate partial melt rich in SiO_2 and with minor MgO and S is present. As temperature increases, the amount of silicate melt increases due to the melting of the feldspar, SiO_2 , and pyroxene (including the Fe,Cr,Ca-rich pyroxene) components. This Fe,Cr,Ca-rich pyroxene is most likely a nonequilibrium form of enstatite. A similar phase is found in many E3–4 chondrites (Weisberg *et al.*, 1994) and is clearly subordinate to enstatite. At 1200–1300 °C, SiO_2 appears to have crystallized from the silicate melt. Increasing enstatite grain sizes

and the presence of forsterite suggests co-crystallization of enstatite and forsterite from the melt between 1400–1450 °C. The spherulitic texture of the 1500 °C suggests quenching of a total melt.

The compositional changes in the silicate melt observed with increasing temperature reflect both the melting behavior of various phases (*e.g.*, the melting temperature and proportions) and transfer of elements between the various melt phases. At low temperature, high Na_2O and Al_2O_3 concentrations in the silicate melt reflect early melting of plagioclase. Decreasing Na_2O in the silicate melt from 1100–1300 °C and its absence above 1300 °C is caused by volatilization. Concentration of Al_2O_3 remains constant to 1425 °C and then decreases. It is unclear why Al_2O_3 remains constant after all plagioclase, the only source of Al_2O_3 in the meteorite, has melted. We note that the experimental charge is not in contact with the alumina crucible that contains the solid metal buffer. With increasing temperature, the abundance of MgO, CaO, and S increase (Table 5, Fig. 8). There are numerous sources for these elements, including oldhamite

(Ca,S), niningerite (Mg,S), plagioclase (Ca), and enstatite (Mg). The presence of abundant S in the silicate melt (≥ 4 wt%) at temperatures above 1400 °C strongly suggests exchange of S between the sulfide and silicate melts, and some of the Ca and Mg in the silicate melt may have also originated as sulfides. At 1500 °C, silicates in Indarch are totally molten, and the S concentration in the melt (4.5 wt%) is comparable to that in the bulk nonmetallic fraction of Indarch (4.1 wt%) (Keil, 1968). The FeO concentration in the silicate melt is low in all charges, which is consistent with their reduced nature.

DISCUSSION

Origin of Aubritic Oldhamite

An interesting outcome of these experiments is that we did not identify any metal or sulfide particles with compositions comparable to those in Indarch (Keil, 1968). Although low-temperature melting of the sulfide component is consistent with low-temperature eutectics

TABLE 4. Quenched liquid sulfide compositions reported in elemental weight percent.

| T | N | Fe | Ni | Mg | Ca | Cr | Mn | Ti | S | Total |
|------|----|-------------|-------------|-------------|-------------|-------------|-------------|-------------|-------------|--------|
| 1500 | 4 | 5.99 (0.88) | ND | BD | BD | 9.25 (1.1) | 46.6 (1.7) | 1.70 (0.25) | 34.5 (0.57) | 98.96 |
| 1425 | 8 | 57.0 (1.9) | 0.89 (0.12) | 0.07 (0.02) | BD | 2.85 (0.90) | 1.64 (0.31) | 0.67 (0.66) | 35.8 (0.31) | 98.94 |
| | 11 | 38.1 (1.9) | 0.12 (0.10) | 2.51 (0.48) | 1.76 (0.33) | 2.49 (0.72) | 17.0 (1.4) | 0.30 (0.16) | 37.0 (0.28) | 99.28 |
| 1400 | 6 | 55.9 (1.2) | 1.26 (0.30) | 0.08 (0.02) | BD | 4.09 (0.40) | 1.33 (0.16) | 0.76 (0.39) | 36.5 (0.32) | 99.95 |
| | 8 | 35.5 (3.1) | 0.30 (0.25) | 3.59 (0.79) | 2.62 (0.78) | 3.33 (0.84) | 15.7 (2.7) | 0.25 (0.11) | 37.8 (0.33) | 99.09 |
| 1300 | 8 | 52.6 (1.0) | 1.01 (0.24) | 0.17 (0.03) | BD | 6.41 (0.68) | 1.14 (0.10) | 0.57 (0.20) | 36.8 (0.25) | 98.71 |
| | 6 | 33.9 (2.3) | 0.26 (0.13) | 5.55 (0.58) | 4.92 (0.39) | 3.85 (0.61) | 12.8 (2.2) | 0.08 (0.06) | 38.4 (0.53) | 99.75 |
| 1200 | 14 | 57.0 (1.0) | 1.55 (0.70) | 0.11 (0.4) | BD | 2.31 (0.47) | 0.67 (0.12) | 0.54 (0.35) | 36.5 (0.43) | 98.71 |
| | 8 | 25.6 (2.5) | 0.07 (0.1) | 11.5 (1.3) | 12.4 (0.6) | 2.36 (0.17) | 7.67 (0.64) | 0.14 (0.04) | 41.6 (0.4) | 101.34 |
| | 3 | 34.1 (0.8) | 0.15 (0.03) | 7.83 (1.40) | 8.78 (0.71) | 1.84 (0.16) | 8.24 (1.25) | 0.15 (0.03) | 40.0 (0.48) | 101.05 |
| 1100 | 5 | 57.4 (0.9) | 0.93 (0.30) | 0.07 (0.03) | BD | 2.61 (0.62) | 0.92 (0.14) | 0.41 (0.23) | 36.6 (0.54) | 98.98 |
| | 5 | 27.9 (0.5) | 0.08 (0.04) | 6.84 (0.19) | 10.4 (0.19) | 3.53 (0.29) | 12.1 (0.2) | 0.20 (0.04) | 39.9 (0.21) | 100.95 |
| 1000 | 5 | 58.1 (2.4) | 0.78 (0.26) | 0.11 (0.03) | 0.08 (0.07) | 2.82 (0.92) | 0.93 (0.21) | 0.53 (0.39) | 36.6 (0.39) | 99.95 |
| | 12 | 38.1 (0.9) | 0.06 (0.04) | 3.58 (0.15) | 4.79 (0.13) | 4.84 (0.65) | 9.58 (0.25) | 0.22 (0.04) | 38.8 (0.38) | 99.97 |

Average ($\pm 1\sigma$). T = temperature in °C. N = number of analyses. ND = not determined. BD = below detection limit (typically 0.03 wt%).

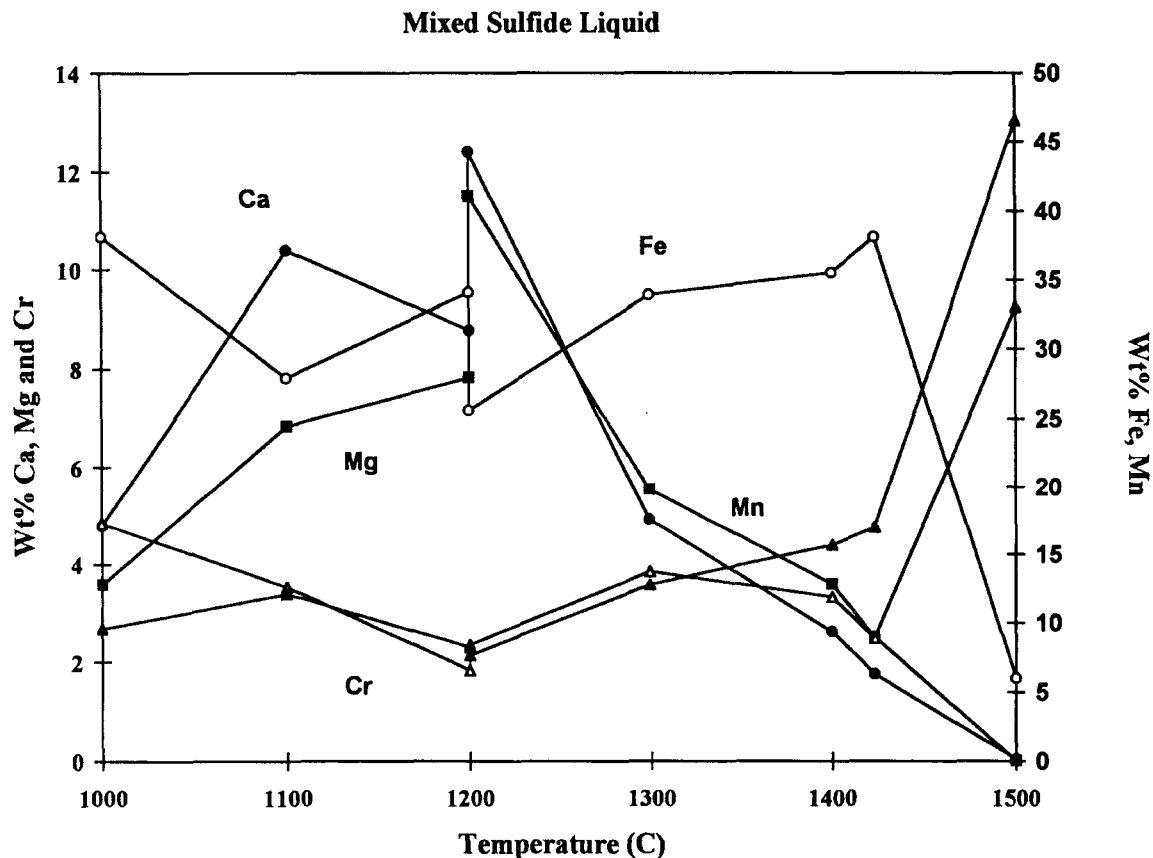


FIG. 7. Temperature vs. average elemental abundance for the mixed sulfide liquid. Iron and Mn are plotted on the right axis and all other elements are plotted on the left axis. At 1200 °C, two mixed sulfides melts of slightly different composition were observed. The cause of the complementary variations of Fe, Mn, and Cr with Mg and Ca in the sulfide melt is unclear but may reflect exchange of Ca and Mg between sulfide and silicate melts or the change in the buffer (V vs. Cr).

in the Fe–FeS (988 °C; Kullerud, 1963), FeS–CaS (1130 °C; Vogel and Heumann, 1941), and FeS–MnS systems (1164 °C; Shibata, 1928), the absence of metal of comparable composition is more surprising. The Fe–FeS cotectic melt should contain ~85 wt% FeS and, thus, abundant residual metal should remain after metal–sulfide melting. One possibility is that residual metal compositionally re-equilibrated at these temperatures. We suggest, instead, that all of the metal melted at low temperatures. This is supported by both the compositions and the grain sizes and shapes of the metal grains in the 1000 °C charge, which are substantially coarser and more rounded than in the powder prior to the experiments. If we are correct, it suggests that phase relations in the Fe–FeS–CaS–MnS system involve much higher proportions of metal than in the Fe–FeS system, an assertion that has yet to be experimentally tested.

The absence of residual sulfides suggests that all sulfides, not just troilite, participate in melting along the Fe–FeS cotectic. Although melting begins at 988 °C in a Ni-free system (Kullerud, 1963), Fogel *et al.* (1989) estimated incorporation of Si in the metal and the presence of other sulfide phases would depress the metal–sulfide melting temperature to ~950 °C. Melting of all sulfides at temperatures as low as 1250 °C was suggested by Fogel *et al.* (1996), based on experiments down to this temperature. We suggest that complete melting of all sulfides and metal

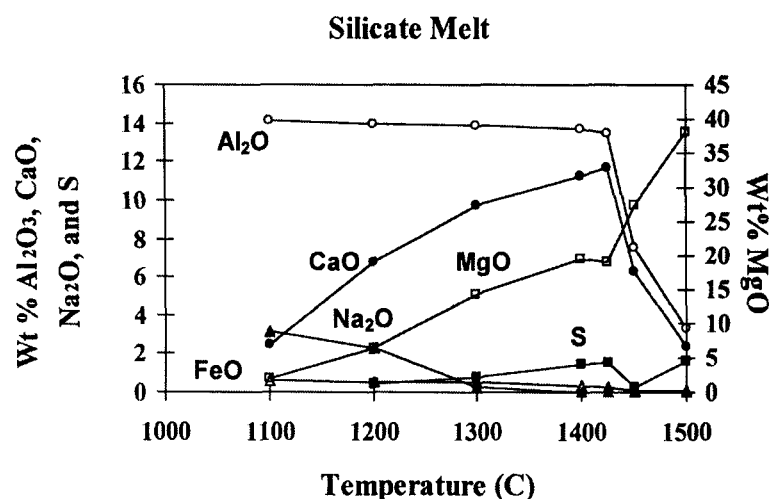


FIG. 8. Temperature vs. average oxide abundance for the silicate melt. Magnesium oxide is plotted on the right axis and all other oxides are plotted on the left axis. The compositional changes in the silicate melt observed with increasing temperature reflect both the melting behavior of various phases (e.g., the melting temperature and proportions) and transfer of elements between the various melt phases. The FeO concentration in the silicate melt is low in all charges, which is consistent with their reduced nature.

TABLE 5. Summary of silicate-melt compositions reported in elemental weight percent.

| T | N | SiO ₂ | TiO ₂ | Al ₂ O ₃ | Cr ₂ O ₃ | FeO | MnO | MgO | CaO | Na ₂ O | K ₂ O | S | Total | O=S | Total |
|------|----|------------------|------------------|--------------------------------|--------------------------------|-------------|-------------|-------------|-------------|-------------------|------------------|-------------|--------|------|--------|
| 1500 | 22 | 54.7 (0.6) | 0.15 (0.03) | 3.29 (0.37) | BD | 0.12 (0.05) | 0.43 (0.10) | 38.1 (1.0) | 2.37 (0.34) | BD | BD | 4.47 (0.22) | 103.81 | 2.24 | 101.58 |
| 1450 | 14 | 57.8 (0.7) | 0.28 (0.03) | 7.51 (0.68) | 0.06 (0.05) | 0.10 (0.03) | 0.34 (0.05) | 27.3 (1.0) | 6.27 (0.48) | BD | BD | 0.72 (0.36) | 100.39 | 0.36 | 100.03 |
| 1425 | 15 | 52.7 (0.8) | 0.21 (0.07) | 13.5 (1.1) | BD | 0.25 (0.06) | 0.12 (0.05) | 19.1 (1.5) | 11.7 (0.5) | BD | BD | 4.36 (0.29) | 101.95 | 2.18 | 99.77 |
| 1400 | 16 | 52.4 (1.8) | 0.16 (0.04) | 13.7 (1.9) | BD | 0.32 (0.18) | 0.19 (0.08) | 19.5 (3.0) | 11.3 (1.9) | BD | BD | 4.14 (0.71) | 101.75 | 2.07 | 99.68 |
| 1300 | 17 | 59.3 (1.0) | BD | 13.9 (0.6) | 0.09 (0.06) | 0.50 (0.15) | 0.07 (0.03) | 14.3 (1.1) | 9.73 (0.32) | 0.23 (0.03) | 0.08 (0.01) | 2.12 (0.09) | 100.27 | 1.06 | 99.21 |
| 1200 | 17 | 67.2 (1.1) | BD | 14.0 (0.6) | BD | 0.55 (0.20) | BD | 6.48 (1.30) | 6.79 (0.41) | 2.31 (0.08) | 0.46 (0.02) | 1.28 (0.08) | 99.19 | 0.64 | 98.55 |
| 1100 | 6 | 75.5 (0.8) | BD | 14.1 (0.3) | BD | 0.56 (0.14) | BD | 1.92 (0.26) | 2.44 (0.33) | 3.10 (0.19) | 0.71 (0.03) | 0.57 (0.02) | 98.97 | 0.29 | 98.69 |

Average ($\pm 1\sigma$). T = temperature in °C. N = number of analyses. BD = below detection limits (typically 0.04 wt%). P₂O₅ is below detection limits in all charges. O=S = S in the silicate melt is likely complexed with Ca and/or Mg (Fogel *et al.*, 1996). We calculated the molar equivalent of S and O and subtracted the mass of this O from the total.

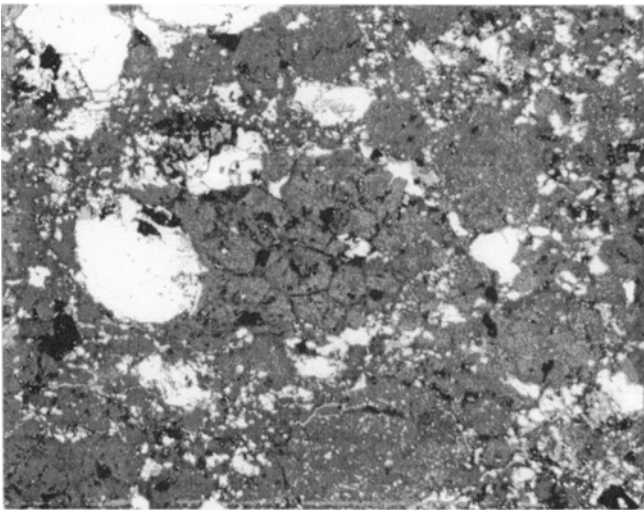


FIG. 9. Reflected light photomicrograph of a porphyritic pyroxene chondrule in the ALH 84250 (EH3) chondrite with large metal-sulfide particles on the surface of the silicate sphere. These metal-sulfide particles probably migrated to the surface of the chondrule under the influence of surface tension when the silicate portion of the chondrule was highly molten. This same effect was clearly seen in our experimental charges. Surficial metal blebs could have been lost during chondrule collisions, depleting some chondrules in metal. Field of view is 1.3 mm.

actually occurs at or below 1000 °C. Earlier assertions of a relic origin for aubritic oldhamite (Kurat *et al.*, 1992; Lodders, 1995, 1996a,b; Lodders *et al.*, 1993; Floss and Crozaz, 1993), based on the argument that oldhamite would survive igneous processing, are not consistent with these observations.

As noted earlier, significant S dissolves within the silicate melt at the low O fugacities appropriate to aubrite formation (Dickinson and Lofgren, 1992; Fogel *et al.*, 1996; McCoy *et al.*, 1997). Fogel *et al.* (1996) first argued that this S is bound with Ca and/or Mg in the silicate melt and, upon cooling, might crystallize oldhamite. This provides a mechanism for the formation of aubritic oldhamite. It appears that we actually see small calcium sulfides crystallizing from the high-temperature (1400–1500 °C) melts upon cooling. Clearly, cooling runs at slower rates are needed to understand the possible crystallization of sulfides from the silicate melt. Such experiments are planned.

Segregation of Metal-Sulfide Melts

The segregation of metal and sulfide in these experiments may have direct applications to enstatite meteorites. Our loose aggregate of metal, sulfide, and silicates in a range of sizes is probably similar to that of chondrule precursors, which contained a melange of phases of varying sizes, including chondrule fragments and relic grains from previous generations of chondrules (Jones, 1996; Lofgren and Le, 1998). Our observations of melt agglomeration and migration to the surface is akin to that seen in other experiments (*e.g.*, Connolly and Hewins, 1996) and inferred for natural chondrules (Zanda *et al.*, 1994).

What is the driving force for this melt migration? Several possibilities exist including surface tension effects, experimental complications, gravitational segregation, and formation of melt networks. The most likely cause for melt migration is surface tension effects, given the high surface/volume ratio of these charges. Indeed, the dispersion of metal-sulfide blebs around the entire surface of the silicate sphere (Fig. 1d) argues for surface tension and against gravitational segregation as a driving force for melt migration. Once silicate partial melting reaches or exceeds 50% in our experi-

ments, metal–sulfide melt migration is extremely efficient, forming spheres on the surface of the charge. This same process operated in molten chondrules, where gravitational effects were negligible, as evidenced by a chondrule with surficial metal–sulfide spheres in the EH3 chondrite ALH 84250 (Fig. 9). This metal could be easily separated from the chondrules by collision between chondrules and account for some of the metal loss observed in chondrules, as suggested by Zanda *et al.* (1994). As Grossman (1996) points out, however, simple loss of metal from chondrules in this manner cannot explain the metal–silicate fractionation observed in chondrites. A possible complication to our interpretation of surface tension as the dominant factor is the use of graphite crucibles. Walker and Agee (1988) noted that sulfides have a strong tendency to bond to graphite, possibly complicating our interpretation.

The formation of melt networks in the absence of surface tension is more difficult to evaluate. At 1300 °C, the experimental charge contains branching metal–sulfide particles reminiscent of melt networks. These particles occur even in the center of the charge where surface tension effects might be minimized. Stevenson (1990) suggested that melts with dihedral angles of 60–120° could form networks at melt fractions of ~10–20%. Sulfur in a metallic melt can substantially decrease the surface tension (Dyson, 1963), promoting network formation. Although difficult to measure, we find dihedral angles of 45–90° and a silicate melt fraction of 19 vol% (Table 2) in our 1300 °C experiment. Thus, migration through melt networks could have been an important process in both our experiments and natural systems. This contrasts with the estimates of Taylor (1992), who suggested that silicate melting would have to exceed 50% for efficient metal melt migration but, based that conclusion on a S-free system. Indeed, metal–sulfide melt migration might occur at low degrees of partial melting (10–20%), but efficient metal segregation might require higher degrees of partial melting.

Finally, it should be noted that we did not observe any explosive removal of metal and/or sulfide from the charge of the type predicted by the model of Wilson and Keil (1991) to explain the absence of basaltic melts from the aubrite parent body. This probably results from the high porosity of our experimental charges (Table 2). Any excess pressure generated during melting and expansion of volatiles would be easily compensated by compression of gas in the abundant pores, and explosive discharge of metal and sulfide would not occur.

Phase Relationships between Enstatite Chondrites and Aubrites

We can examine the silicate melt compositions and phase relations in our melting experiments using the phase diagrams for the forsterite–albite–SiO₂ (Schairer and Yoder, Jr., 1961) and forsterite–anorthite–SiO₂ systems. The Fo–Ab–SiO₂ system would seem to be ideal for studying the melting of Indarch, which contains enstatite with only minor FeO, nearly pure albite (Ab_{97.6}), and free SiO₂ (Keil, 1968). A similar approach to predict the ideal melting behavior of enstatite chondrites was used by Fogel *et al.* (1988). However, as we will show, our experiments are only partially explained by phase relationships in this system. Thus, we also discuss our experiments in the context of the Fo–An–SiO₂ system.

Compositions were plotted within the Fo–Ab–SiO₂ and Fo–An–SiO₂ ternaries using Al₂O₃ abundances for Ab and An, MgO abundances for Fo, and excess SiO₂ for SiO₂. As discussed above, our high-temperature experiments experienced significant volatilization and loss of Na. As such, we recognize that the use of the metaluminous Fo–Ab–SiO₂ and Fo–An–SiO₂ systems is not strictly applicable to our peraluminous melts. It is unknown whether the use of such a projection is valid, but we suggest that both systems illustrate the importance of volatilization and elemental exchange. Alternative means of projecting compositions are equally uncertain. For example, it is impossible to calculate the plagioclase component from the CaO content of the silicate melt, because some of the Ca is certainly complexed with S, but the Ca/Mg ratio of the cations complexed with S is unconstrained on either a thermodynamic or experimental basis.

The bulk composition of Indarch silicates (Wiik, 1956) and our experimental silicate melt compositions are plotted in Fig. 10a.

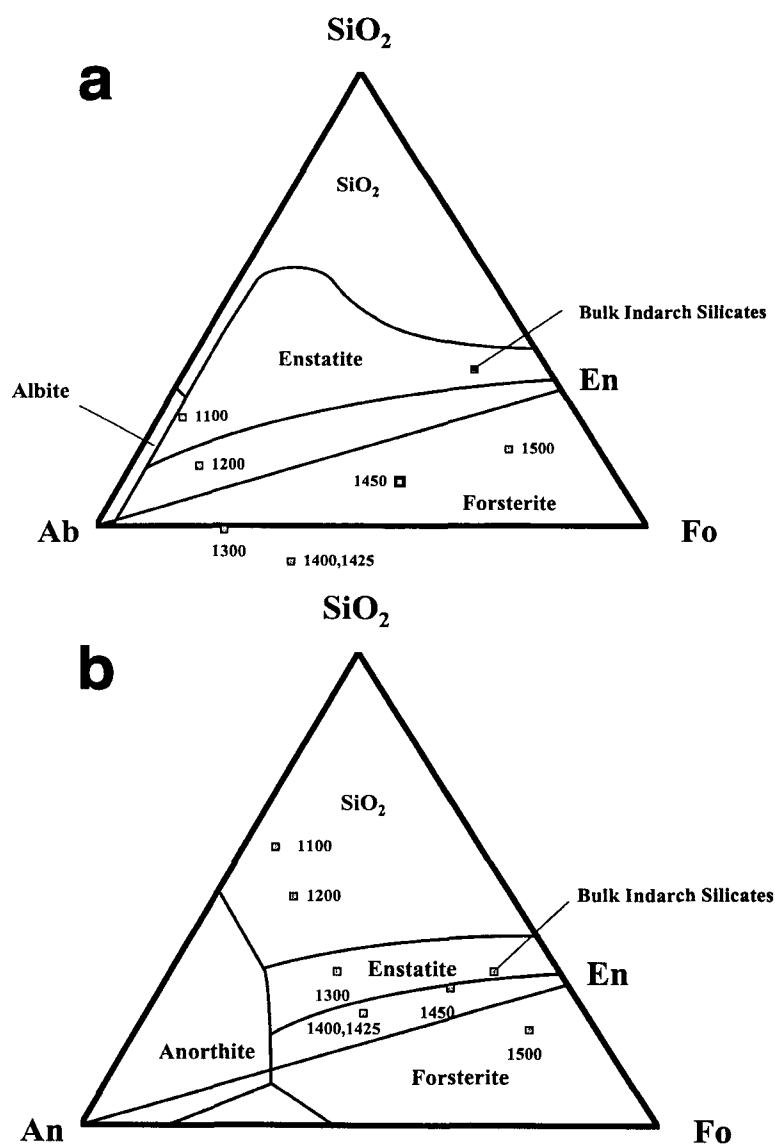


FIG. 10. The bulk composition of Indarch silicates (Wiik, 1956) and our experimental silicate melt compositions are plotted on (a) the Fo–Ab–SiO₂ phase diagram (Schairer and Yoder, Jr., 1961) and (b) the Fo–An–SiO₂ phase diagram (see text for discussion).

Although there are rather large uncertainties in the Indarch bulk silicate composition, it must lie somewhere near the forsterite–enstatite cotectic. The melting of Indarch silicates should start at 1062 °C (En–Ab–SiO₂ peritectic) and proceed to the En–Ab–Fo peritectic (1095 °C), where albite is exhausted. At temperatures >1095 °C, forsterite is formed by incongruent melting of enstatite along the En–Fo cotectic line. Total melting would require temperatures in excess of 1500 °C.

Our experiments are only partially explained by phase relationships in the Fo–Ab–SiO₂ ternary. Consistent with the prediction of initial silicate melting at 1062 °C, silicate partial melts are first found at 1100 °C. Albite plagioclase has melted at this temperature, whereas the more anorthitic plagioclase remains. However, our silicate melt compositions are inconsistent with melting in the Fo–Ab–SiO₂ system above 1100 °C. Rather than follow the Fo–En cotectic to higher temperatures, the 1300–1500 °C melts lie across the plane of silica saturation, and the 1300–1425 °C melts lie across the plane of silica undersaturation. Furthermore, the 1200–1300 °C charges appear to have crystallized quartz, whereas the 1450 °C charge cocrystallized forsterite and enstatite, despite all three being in the forsterite stability field. The deviation from expected behavior can be explained by the volatilization of Na during melting. All of these melts are peraluminous, highly so at 1200 °C and above. Our experiments may be better understood by considering the Fo–An–SiO₂ phase diagram, the calcic analog of the Fo–Ab–SiO₂ system.

If we examine the Fo–An–SiO₂ system, we find that we can better explain both the compositions and coexisting phases in the silicate melts. In contrast to the situation in the sodic system, where the melts were peraluminous, the melts are Al deficient and Ca-enriched in the calcic system. Calcium may well be combined with S to produce calcium sulfide in the silicate melt, a conclusion supported by the apparent crystallization of CaS and the near equality in moles of excess Ca and S in the silicate melts. In the Fo–An–SiO₂ system (Fig. 10b), all melt compositions are shifted to more SiO₂-rich values, because anorthite contains less SiO₂ and more Al₂O₃ than albite. As a result, the 1100 and 1200 °C silicate melt compositions lie within the SiO₂ field, whereas the 1300 °C melt composition is within the enstatite field. Thus, significant Na volatilization during the run forced these melts into the Fo–An–SiO₂ system, with resulting SiO₂ crystallization. Crystallization of SiO₂ from the 1300 °C melt causes the remaining melt to move into the enstatite field. At 1400–1450 °C, the silicate melt compositions lie on the En–Fo cotectic, which is consistent with the cocrystallization of enstatite and forsterite in these samples. The 1500 °C melt composition does not lie either on the phase boundaries or close to the bulk composition of Indarch silicates. Instead, it is shifted away from the Indarch bulk silicates on a line through the SiO₂ apex. We suggest that this reflects the reduction of SiO₂ in the silicate melt to Si in the metallic melt, although we recognize that the exact colinearity of these points in the Fo–An–SiO₂ system might be an artifact of the projection used. Reduction of SiO₂ to Si might also occur in natural systems, although to a lesser extent given the limited supply of reductant in natural systems. Reduction of SiO₂ from the silicate melt would result in the crystallization of forsterite, a phase which is common in aubrites but relatively rare in enstatite chondrites.

CONCLUSIONS

Our experiments suggest some interesting complexities to the melting of enstatite chondrites. Not surprisingly, experimental difficulties with Na volatilization significantly alter the melting and

crystallization behavior of the silicates, and overcoming this problem is a focus of continuing efforts. Despite this problem, however, our work does address some of the most important issues in aubrite petrogenesis discussed earlier. All of the sulfides within the enstatite chondrite melt at a relatively low temperature (1000 °C), prior to silicate melting and volatile loss. This presents substantial difficulties for models that invoke a relic origin for aubritic oldhamite. The metal–sulfide melt might have formed networks and migrated even at relatively low temperatures (1300 °C) and degrees of silicate partial melting (20%). Substantial elemental exchange occurred between different melts (*e.g.*, S between sulfide and silicate, Si between silicate and metal), a feature not observed during experiments at higher *f*O₂. This exchange may help explain the formation of aubrites from known enstatite chondrites. In particular, elemental exchange and subsequent crystallization could cause crystallization of oldhamite from S-rich silicate melts, crystallization of forsterite from Si-undersaturated silicate melts, and crystallization of Ti-rich troilite from a Fe-rich sulfide melt coexisting with an immiscible, mixed sulfide melt. Finally, our experiments suggest that partial melts removed during melting of an enstatite chondrite, depending on temperature, would probably be broadly basaltic (enstatite–plagioclase) but would likely contain substantial amounts of crystallized sulfides. Searches for sulfide-rich clasts may be an effective means to identify such partial melts.

Acknowledgments—We gratefully acknowledge E. Olsen (Field Museum) for providing the Indarch sample for this work. We thank V. Lauer for help in running experiments, T. Gooding for polished thin sections, and E. Jarosewich for assistance in microprobe analyses. Helpful discussions and comments on this manuscript were provided by C. Bertka, H. C. Connolly, Jr., R. A. Fogel, and G. J. Taylor. This work was supported by National Research Council Post Doctoral Fellowships to T.L.D. and T.J.M. and NASA grants NAG 5-4490 (T.J.M.), NAG 5-4345 (T.L.D.), and RTOP 344-31-20-20 (G.E.L.).

Editorial handling: E. R. D. Scott

REFERENCES

- BRETT R. AND KEIL K. (1986) Enstatite chondrites and enstatite achondrites (aubrites) were not derived from the same parent body. *Earth Planet. Sci. Lett.* **81**, 1–6.
- CASANOVA I., KEIL K. AND NEWSOM H. E. (1993) Composition of metal in aubrites: Constraints on core formation. *Geochim. Cosmochim. Acta* **57**, 675–682.
- CLAYTON R. N., MAYEDA T. K. AND RUBIN A. E. (1984) Oxygen isotopic compositions of enstatite chondrites and aubrites. *Proc. Lunar Planet. Sci. Conf.* **15th**, C245–C249.
- CONNOLLY H. C., JR. AND HEWINS R. H. (1996) Constraints on chondrule precursors from experimental data. In *Chondrules and the Proto-planetary Disk* (eds. R. H. Hewins, R. H. Jones and E. R. D. Scott), pp. 129–135. Cambridge Univ. Press, Cambridge, U.K.
- CROZAZ G. AND LUNDBERG L. L. (1995) The origin of oldhamite in unequilibrated enstatite chondrites. *Geochim. Cosmochim. Acta* **59**, 3817–3831.
- DICKINSON T. L. AND LOFGREN G. E. (1992) Melting relations for Indarch (EH4) under reducing conditions (abstract). *Lunar Planet. Sci.* **23**, 307–308.
- DICKINSON T. L., MCCOY T. J. AND LOFGREN G. E. (1998) Melting of Indarch (EH4) powders: Phase relations and element exchange (abstract). *Lunar Planet. Sci.* **29**, #1450, Lunar Planetary Institute, Houston, Texas, USA (CD-ROM).
- DYSON B. F. (1963) The surface tension of iron and some iron alloys. *Trans. Metall. Soc. AIME* **227**, 1098–1102.
- FLOSS C. AND CROZAZ G. (1993) Heterogeneous REE patterns in oldhamite from the aubrites: Their nature and origin. *Geochim. Cosmochim. Acta* **57**, 4039–4057.
- FOGEL R. A., HESS P. C. AND RUTHERFORD M. J. (1988) The enstatite chondrite–achondrite link (abstract). *Lunar Planet. Sci.* **19**, 342–343.
- FOGEL R. A., HESS P. C. AND RUTHERFORD M. J. (1989) Intensive parameters of enstatite chondrite metamorphism. *Geochim. Cosmochim. Acta* **53**, 2765–2746.

- FOGEL R. A., WEISBERG M. K. AND PRINZ M. (1996) The solubility of CaS in aubrite silicate melts (abstract). *Lunar Planet. Sci.* **27**, 371–372.
- GROSSMAN J. N. (1996) Chemical fractionations of chondrites: Signatures of events before chondrule formation. In *Chondrules and the Protoplanetary Disk* (eds. R. H. Hewins, R. H. Jones and E. R. D. Scott), pp. 243–253. Cambridge Univ. Press, Cambridge, U.K.
- JONES R. H. (1996) Relict grains in chondrules: Evidence for chondrule recycling. In *Chondrules and the Protoplanetary Disk* (eds. R. H. Hewins, R. H. Jones and E. R. D. Scott), pp. 163–172. Cambridge Univ. Press, Cambridge, U.K.
- KEIL K. (1968) Mineralogical and chemical relationships among enstatite chondrites. *J. Geophys. Res.* **73**, 6945–6976.
- KULLERUD G. (1963) The Fe–Ni–S system. *Ann. Rep. Geophys. Lab* **67**, 4055–4061.
- KURAT G., ZINNER E. AND BRANDSTATTER F. (1992) An ion microprobe study of an unique oldhamite-pyroxenite fragment from the Bustee aubrite (abstract). *Meteoritics* **27**, 246–247.
- LODDERS K. (1995) Experimental partitioning of rare earth elements between sulfides (FeS, CaS) and silicate melt and applications to enstatite achondrites. *Proc. NIPR Symp. Antarct. Meteorites* **8**, 140–143.
- LODDERS K. (1996a) Oldhamite in enstatite achondrites (aubrites). *Proc. NIPR Symp. Antarct. Meteorites* **9**, 127–142.
- LODDERS K. (1996b) An experimental and theoretical study of rare-earth-element partitioning between sulfides (FeS, CaS) and silicate and applications to enstatite achondrites. *Meteorit. Planet. Sci.* **31**, 749–766.
- LODDERS K., PALME H. AND WLOTZKA F. (1993) Trace elements in mineral separates of the Peña Blanca Spring aubrite: Implications for the evolution of the aubrite parent body. *Meteoritics* **28**, 538–551.
- LOFGREN G. E. AND LE L. (1998) Partial melting of Type 1 chondrule precursor aggregates: An experimental and petrographic study (abstract). *Lunar Planet. Sci.* **29**, #1441, Lunar Planetary Institute, Houston, Texas, USA (CD-ROM).
- LONSDALE J. T. (1947) The Peña Blanca Spring meteorite, Brewster County, Texas. *Am. Mineral.* **32**, 354–364.
- MCCOY T. J., DICKINSON T. L. AND LOFGREN G. E. (1997) Partial melting of Indarch (EH4) from 1000–1500 °C: New insights into igneous processes in enstatite meteorites (abstract). *Lunar Planet. Sci.* **28**, 903–904.
- MCCOY T. J., DICKINSON T. L. AND LOFGREN G. E. (1998) Partial melting of the Indarch (EH4) meteorite: A textural view of melting and melt migration (abstract). *Meteorit. Planet. Sci.* **33** (Suppl.), A100–A101.
- SCHAIER J. F. AND YODER H. S., JR. (1961) The system albite–forsterite–silica. *Carnegie Inst. Washington* **60**, 69–70.
- SHIBATA Z. (1928) Equilibrium diagram of the iron sulphide–manganese sulphide system. *Tech. Rep. Tohoku Imp. Univ.* **7**, 279–289.
- STEVENSON D. J. (1990) Fluid dynamics of core formation. In *Origin of the Earth* (eds. H. E. Newsom and J. H. Jones), pp. 231–249. Oxford Univ. Press, New York, New York, USA.
- TAYLOR G. J. (1992) Core formation in asteroids. *J. Geophys. Res.* **97**, 14 717–14 726.
- TAYLOR G. J., KEIL K., NEWSOM H. AND OKADA A. (1988) Magmatism and impact on the aubrite parent body: Evidence from the Norton County enstatite achondrite (abstract). *Lunar Planet. Sci.* **19**, 1185–1186.
- TAYLOR G. J., KEIL K., MCCOY T., HAACK H. AND SCOTT E. R. D. (1993) Asteroid differentiation: Pyroclastic volcanism to magma oceans. *Meteoritics* **28**, 34–52.
- VOGEL R. AND HEUMANN T. (1941) Das System Eisen-Eisensulfid-Kalziumsulfid. *Archiv Eisenhüttenw.* **15**, 195–199.
- WALKER D. AND AGEE C. B. (1988) Ureilite compaction. *Meteoritics* **23**, 81–91.
- WATTERS T. R. AND PRINZ M. (1979) Aubrites: Their origin and relationship to chondrites. *Proc. Lunar Planet. Sci. Conf.* **10th**, 1073–1093.
- WEISBERG M. K., PRINZ M., AND FOGEL R. A. (1994) The evolution of enstatite and chondrules in unequilibrated enstatite chondrites: Evidence from iron-rich pyroxene. *Meteoritics* **29**, 362–373.
- WHELOCK M. M., KEIL K., FLOSS C., TAYLOR G. J. AND CROZAS G. (1994) REE geochemistry of oldhamite-dominated clasts from the Norton County aubrite: Igneous origin of oldhamite. *Geochim. Cosmochim. Acta* **58**, 449–458.
- WIK H. B. (1956) On regular discontinuities in the composition of meteorites. *Comment. Phys. Mat.* **34**, 135–145.
- WILSON L. AND KEIL K. (1991) Consequences of pyroclastic volcanism on small Solar System bodies: The case of the missing basalts on the aubrite parent body. *Earth Planet. Sci. Lett.* **104**, 505–512.
- ZANDA B., BOUROT-DENISE M., PERRON C. AND HEWINS H. (1994) Origin and metamorphic redistribution of silicon, chromium, and phosphorus in the metal of chondrites. *Science* **265**, 1846–1849.

APPENDIX

All of the charges were prepared by placing ~160 mg of loose Indarch powder into a graphite crucible with 9 mm outer diameter and 5 mm inner diameter, producing charges ~5 mm in diameter. In this section, we document (a) large-scale changes to the charge with increasing temperature, (b) textural changes to the silicate component, and (c) textural changes to the metal–sulfide component.

Charge TD-286 (1000 °C, 24 h, V buffer)

The incoherent charge consists of chondrule and mineral fragments typically <100 µm across and always <500 µm. The charge was impregnated with epoxy within the graphite crucible. Metal particles reach 300 µm, and sulfide particles reach 100 µm.

Abundant enstatite, plagioclase, and minor to rare Fe,Ca,Cr-rich pyroxene and SiO₂ are present. Enstatite occurs as <100 µm grains that commonly exhibit polysynthetic twinning. Chondrule fragments occur throughout the charge. Smaller plagioclase grains occur interstitially to enstatite. No silicate partial melts were observed.

Metallic and sulfide melts are found throughout the charge as irregularly shaped grains, both as compound grains and separately. The FeNiSi metallic melts occasionally reach 300 µm. Sulfide particles are typically <100 µm in diameter and the two sulfide melts (Fe-rich and FeMgMnCaCr-rich) occur as distinct grains. No relic sulfides were observed optically or during microprobe analyses. Very small particles of all three phases are also found throughout the silicates, sometimes infilling cracks. Graphite laths are present but may be fragments of the graphite crucible.

Charge TD-291 (1100 °C, 24 h, V buffer)

The overall texture of this charge is essentially indistinguishable from TD-286 (1000 °C).

The silicates include abundant enstatite, now-solidified silicate melt, minor amounts of Fe,Ca,Cr-rich pyroxene and plagioclase, and extremely rare forsterite and SiO₂, the latter three typically associated with silicate melt. Enstatite occurs as <100 µm grains that commonly exhibit polysynthetic twinning. Interstitial silicate melt pockets reach 10 µm.

Metal and sulfide are found throughout the charge as extremely irregularly shaped grains, both as compound grains and separately. The FeNiSi metal particles reach 300 µm. Troilite particles are extremely irregularly shaped, up to 100 µm in maximum dimension, and rarely contain skeletal FeMgMnCaCr-rich sulfides. More typically, FeMgMnCaCr-rich sulfides occur as distinct grains, which reach 40 µm in diameter and often have convex borders with adjacent troilite, indicative of two immiscible melts. Very small particles of all three phases are also found throughout the silicates. Despite intensive searches, no relic sulfides were encountered during microprobe analyses.

Charge TD-261 (1200 °C, 24 h, Cr buffer)

The charge is coherent. It is turned on its side within the crucible but retains the crucible's shape. However, it is not compact, with numerous cracks cross-cutting the specimen. Metal and sulfide particles are small (<500 µm) and dispersed throughout the silicate host.

Silicates include enstatite, Fe,Ca,Cr-rich pyroxene, SiO₂, and now-solidified silicate melt. Silicates display a wide range of grain sizes but are generally <100 µm. Fragments of relic chondrules are also observed. Polysynthetic twinning of enstatite is common. Minor Fe,Ca,Cr-rich pyroxene was identified in the electron microprobe. Irregular, interstitial patches of silicate melt up to 30 µm across contain subhedral to skeletal SiO₂ grains <10 µm across.

Metal and sulfide are found throughout the charge as extremely irregularly shaped grains, both as compound grains and separately. Large metal particles (up to 500 µm) are a two-phase intergrowth (an FeNiSi metal network with interstitial C-bearing metal) and typically contain small (1–5 µm) troilite grains. Rare P-rich metal was observed during microprobe analyses. At the edge of many metal grains, the C-bearing metal is replaced by irregular voids. Troilite particles are extremely irregularly shaped, up to 150 µm in maximum dimension, and sometimes contain skeletal FeMgMnCaCr-rich sulfides. More typically, FeMgMnCaCr-rich sulfides occur as distinct grains, which reach 80 µm in diameter and often have convex borders with adjacent troilite, indicative of two immiscible melts. Very small particles of all three phases are

also found throughout the silicates. No relic sulfides were observed during microprobe analyses.

Charge TD-278 (1300 °C, 24 h, Cr buffer)

The charge is ~5 mm across and is still contained within and shaped to match the graphite crucible. The charge appears coherent but not compact. Large cracks cross cut the entire charge. Metal and sulfide particles are small (≤ 0.5 mm) and dispersed throughout the silicate host.

The silicates include enstatite, SiO_2 , and now-solidified silicate melt. Silicates are generally quite fine grained ($< 100 \mu\text{m}$), with some larger grains and chondrule fragments present. Polysynthetic twinning of enstatite is common. Irregular, interstitial patches of silicate melt up to $50 \mu\text{m}$ across contain subhedral to skeletal SiO_2 grains $< 20 \mu\text{m}$ across.

Metal and sulfide are found throughout the charge as irregularly shaped grains, both as compound particles and separately. Large metal particles are a two-phase intergrowth (an FeNiSi metal network with interstitial C-bearing metal), typically contain small ($1\text{--}5 \mu\text{m}$) troilite grains, and are sometimes rimmed by sulfides. Metal also occurs as small particles, stringers, and dendrites within larger troilite particles. In some parts of the charge, the irregular metal particles may form a continuous network in three dimensions. Larger troilite particles often contain skeletal and cruciform FeMgMnCaCr-rich sulfide. Very small particles of all three phases are also found throughout the silicates. No relic sulfides were observed during microprobe analyses.

Charge TD-269 (1400 °C, 24 h, Cr buffer)

The charge is a coherent silicate sphere with numerous, rounded $1\text{--}3$ mm blebs of metal and sulfide.

The silicates are enstatite, olivine, and now-solidified silicate melt. Small ($< 100 \mu\text{m}$) striated enstatites are evenly dispersed throughout the sphere. A single large ($800 \mu\text{m}$) lath of enstatite is also present. Interstitial finely crystalline silicate melt contains small gray sulfides. These sulfides, which are $< 2 \mu\text{m}$ in diameter, could not be reliably analyzed. Olivine grains reach $200 \mu\text{m}$ in length, range in shape from skeletal to euhedral, and are found both rimming the silicate sphere and as scattered, isolated grains within the sphere.

Metal and sulfides occur throughout the charge as compound particles 0.5 to 3 mm in diameter. Metal is dominantly FeNiSi metal with interstitial C-bearing metal. In the center of the charge, metal occurs as a rounded sphere with a shell of sulfides. The sulfides are dominantly Fe-rich with included small ($\sim 5 \mu\text{m}$ across) dendritic metal particles, skeletal or cruciform gray FeMnMgCaCr-rich sulfide. The latter often contains tiny (1 by $5 \mu\text{m}$) needles of Fe-rich sulfide. Near the edge of the charge, both the sulfide and interstitial C-rich metal are largely absent. The absence of C-rich metal produces a skeletal appearance in the metal particles. No relic sulfides were observed.

Charge TD-262 (1425 °C, 20 h, Cr buffer)

The charge is a coherent silicate sphere with numerous, rounded $1\text{--}2$ mm blebs of metal and sulfide.

The silicates are dominantly small ($< 100 \mu\text{m}$) striated enstatites that are evenly dispersed throughout the sphere. Larger enstatites also occur. Interstitial finely crystalline silicate melt pockets up to $300 \mu\text{m}$ across contain small gray sulfides. These sulfides, which are $< 2 \mu\text{m}$ in diameter, could not

be reliably analyzed. Rimming the sphere are olivine grains that reach $200 \mu\text{m}$ in length and often exhibit embayments.

Metal and sulfides occur throughout the charge as compound particles $0.7\text{--}2$ mm in diameter. Metal is dominantly FeNiSi metal with interstitial C-bearing metal. In the center of the charge, metal occurs as a rounded sphere with a shell of sulfides. The sulfides are dominantly Fe-rich with included small ($\sim 5 \mu\text{m}$ across) dendritic metal particles, skeletal or cruciform gray FeMnMgCaCr-rich sulfide. The latter often contains tiny (1 by $5 \mu\text{m}$) needles of Fe-rich sulfide. Near the edge of the charge, both the sulfide and interstitial C-rich metal are largely absent, although sulfide particles up to $80 \mu\text{m}$ in diameter are found within metal. The absence of C-rich metal produces a skeletal appearance in the metal particles. No relic sulfides were observed.

Charge TD-285 (1450 °C, 16 h, Cr buffer)

The charge is a silicate sphere with $1\text{--}2.5$ mm metallic spheres occurring on the surface of the silicate sphere. The largest metallic sphere separated from the charge upon cooling, leaving an indentation in the silicate sphere.

The silicate sphere consists of skeletal crystals of striated enstatite, skeletal and barred olivine crystals, and fine-grained or feather-textured crystallized silicate melt. Striated enstatite reaches > 2 mm in maximum dimension. The largest such grain is found rimming the concave surface from which the largest metal particle was removed. Olivine is found as multiple sets of barred crystals that reach several millimeters in maximum dimension. Individual bars often exhibit skeletal textures. Quenching of the silicate melt has produced fine-grained and feathery-textured crystallites, as well as glass interstitially to the large silicates. No relic silicates are apparent.

The metallic spheres are composed predominantly of FeNiSi metal islands up to $20 \mu\text{m}$ in diameter with rare interstitial patches of P-rich metal or, more commonly, empty cracks. Metal particles $1\text{--}10 \mu\text{m}$ in diameter are found within all of the silicate phases. No sulfides have been observed in any of several slices of this charge.

Charge TD-284 (1500 °C, 4 h, Cr buffer)

The charge is a silicate sphere with $1\text{--}2$ mm metallic spheres occurring on the surface of the silicate sphere. The largest metallic sphere separated from the charge upon cooling, leaving an indentation in the silicate sphere.

The silicate portion of the sphere is composed entirely of radiating spherulites that range in size from $50\text{--}500 \mu\text{m}$ in diameter. The spherulites are too fine grained to reliably analyze individual phases but appear to be composed of radiating needles of enstatite that are submicron in width. The areas between the enstatites are silicate melt that contain extremely minute sulfides. The silicate assemblage appears to have formed during quenching of a total melt and no relic silicates are observed.

The $1\text{--}2$ mm metallic spheres are composed predominantly of FeNiSi metal islands up to $20 \mu\text{m}$ in diameter with rare interstitial patches of P-rich metal or, more commonly, empty cracks and voids. In the center of the largest metal particle are rare small ($< 10 \mu\text{m}$) skeletal or cruciform Mn,Cr,Fe,Ti sulfides that sometimes occur in small clusters. All metal or sulfide particles within the silicate sphere are submicron in size.